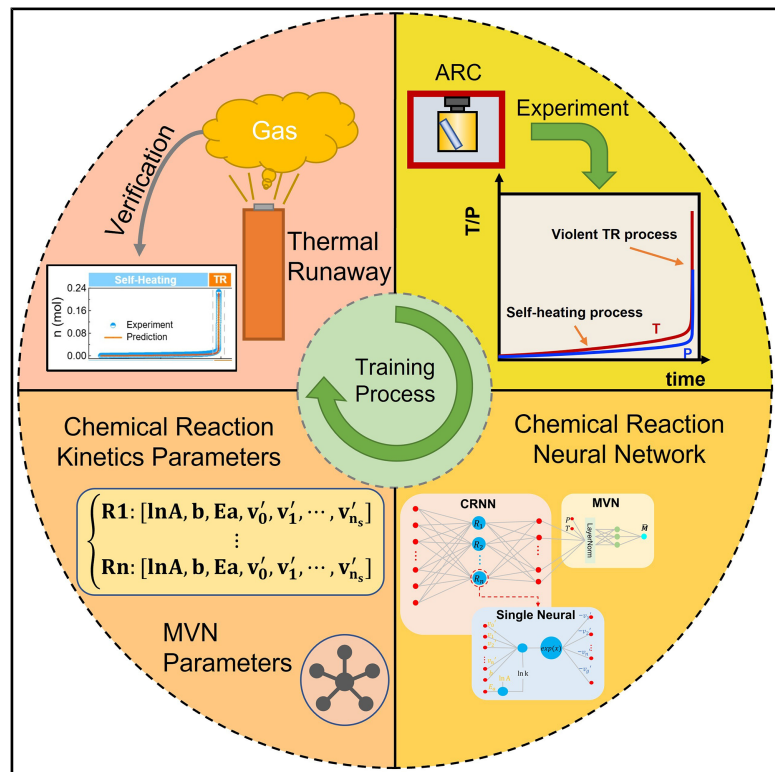


# Chemical reaction neural networks to map lithium-ion battery thermal runaway gas generation

## Graphical abstract



## Authors

Jiabo Zhang, Changsheng Ma,  
Shuaiqi Liu, ..., Peng Han, Zhen Huang,  
Dong Han

## Correspondence

[zhangjiabo@sjtu.edu.cn](mailto:zhangjiabo@sjtu.edu.cn) (J.Z.),  
[dong\\_han@sjtu.edu.cn](mailto:dong_han@sjtu.edu.cn) (D.H.)

## In brief

Here, Zhang et al. extended a CRNN model that autonomously maps gas generation reaction pathways in lithium-ion battery thermal runaway. The first-ever kinetic model bridges modeling gaps, enabling accurate predictions of safety-critical parameters such as gas generation rates and amounts, advancing the understanding of thermal safety in LIBs.

## Highlights

- CRNN model is employed to autonomously explore the unknown reaction pathway
- A first-ever chemical kinetic mechanism related to LIB TR gas generation is established
- Learned pathways and kinetic parameters align well with experimental observations
- Gas generation rates and amounts are accurately predicted across cells with varied SOCs



Article

# Chemical reaction neural networks to map lithium-ion battery thermal runaway gas generation

Jiabo Zhang,<sup>1,2,6,\*</sup> Changsheng Ma,<sup>3</sup> Shuaiqi Liu,<sup>1</sup> Qianzhen Guo,<sup>1</sup> Shaoyan Liu,<sup>4</sup> Peng Han,<sup>5</sup> Zhen Huang,<sup>1,2</sup> and Dong Han<sup>1,2,\*</sup>

<sup>1</sup>Key Laboratory for Power Machinery and Engineering, Ministry of Education, Shanghai Jiao Tong University, Shanghai 200240, China

<sup>2</sup>Shanghai Non-carbon Energy Conversion and Utilization Institute, Shanghai 200240, China

<sup>3</sup>School of Information Science and Engineering, Lanzhou University, Lanzhou 730000, China

<sup>4</sup>China-UK Low Carbon College, Shanghai Jiao Tong University, Shanghai 200240, China

<sup>5</sup>Department of Computer Science, University of Electronic Science and Technology of China, Chengdu 610054, China

<sup>6</sup>Lead contact

\*Correspondence: [zhangjiabo@sjtu.edu.cn](mailto:zhangjiabo@sjtu.edu.cn) (J.Z.), [dong\\_han@sjtu.edu.cn](mailto:dong_han@sjtu.edu.cn) (D.H.)

<https://doi.org/10.1016/j.xcpr.2025.102563>

## SUMMARY

The widespread application of lithium-ion batteries in electric vehicles is hindered by safety concerns, notably thermal runaway. Understanding gas generation during thermal runaway is crucial for battery safety design, early fault detection, and fire hazard assessment, but existing kinetic models remain inadequate. We investigate gas generation behavior of 18650-type  $\text{LiNi}_{1/3}\text{Co}_{1/3}\text{Mn}_{1/3}\text{O}_2$  cells across varied states of charge, constructing a training dataset to develop a chemical reaction neural network model that autonomously explores unknown reaction pathways and corresponding chemical kinetic parameters. By incorporating an additional non-linear neural network to predict the mean molar weight of generated gases, the model trains a chemical kinetic mechanism comprising 7 species and 16 reactions. The resulting mechanism accurately predicts key parameters, including gas generation rates and amounts, during thermal runaway. This methodology addresses the current limitations in thermal runaway gas prediction, providing a robust framework for enhancing battery safety.

## INTRODUCTION

Due to their high energy density, exceptional cycling performance, and low self-discharge rate, lithium-ion batteries (LIBs) have become one of the most widely used power sources in electric vehicles.<sup>1,2</sup> However, safety concerns related to thermal runaway (TR), resulting from uncontrolled side reactions among the active materials within the cells, significantly constrain the development of LIBs.<sup>3–5</sup> During TR, a substantial quantity of combustible gases is generated, elevating the risks of fire and explosion.<sup>6,7</sup>

Research focusing on gas generation during the TR process holds immense practical significance.<sup>8–14</sup> For example, Jin et al.<sup>15</sup> conducted *in situ* optical diagnostics to detect lithium dendrite growth and the resultant gas composition, identifying  $\text{H}_2$  from the spontaneous reaction between lithium and polymer binders as an early warning indicator. Moreover, Jia et al.<sup>16</sup> examined the effects of cathode materials (e.g.,  $\text{LiFePO}_4$  [LFP],  $\text{LiMn}_2\text{O}_4$  [LMO], and  $\text{LiNi}_{0.8}\text{Co}_{0.1}\text{Mn}_{0.1}\text{O}_2$  [NCM]) on the gas release behavior in fully charged LIBs. The results revealed that the order of gas release amount before the cell approached the separator collapse temperature was LFP > NCM > LMO cells. Such insights are crucial for battery shell strength design. On the other hand, Zhang et al.<sup>17</sup> utilized Raman spectroscopy

to detect gas components in venting gas across cells with different states of charge (SOCs) and compared their explosion limits. It was observed that an increased SOC led to a higher risk of explosion after TR.

To deepen comprehension of the LIB TR process, more insights into the reaction kinetics are necessary.<sup>11,18</sup> To this end, Richard and Dahn<sup>19</sup> pioneered the use of Arrhenius-like expressions in describing the heat release behavior resulting from side reactions during TR. Subsequently, Kim et al.<sup>20</sup> defined the side reaction of TR as a four-step process, namely the solid electrolyte interface (SEI) decomposition reaction, the negative-solvent reaction, the positive-solvent reaction, and the electrolyte decomposition reaction. Building upon these advancements, Ren et al.<sup>21</sup> fitted the thermal kinetic parameters of TR reactions and successfully predicted the temperature evolution of LIBs in oven tests. However, these models focus solely on the heat generation of the cells and lack the capability to predict gas generation behavior, signifying an existing gap in research. Notably, recent studies by Mao et al.<sup>22</sup> and Guo et al.<sup>23</sup> revealed a non-linear relationship between gas generation rate and heat generation rate, underscoring the necessity for a novel chemical kinetic mechanism.

However, the LIB TR process is inherently complex and multi-phase, presenting challenges in identifying the intermediate



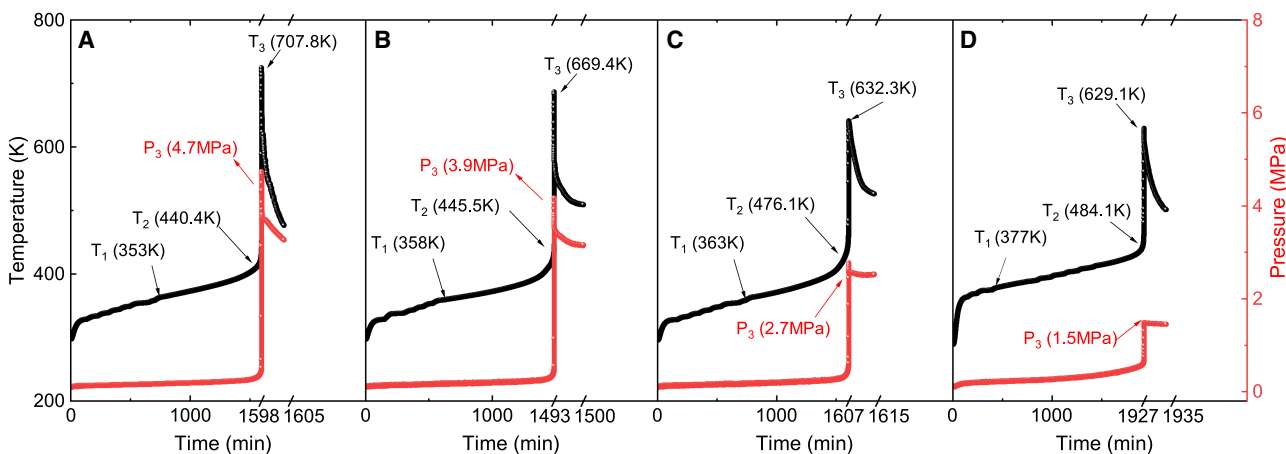


**Figure 1. Evolution of temperature and pressure for NCM cells with different SOCs**

(A) Evolution of temperature and pressure at 120% SOC.

(B) Evolution of temperature and pressure at 100% SOC.

(C) Evolution of temperature and pressure at 70% SOC.

(D) Evolution of temperature and pressure at 50% SOC.

See Zhang et al.<sup>34</sup>

species and underlying reaction pathways for gas generation via conventional methods. To autonomously discover unknown reaction networks, Ji and Deng<sup>24</sup> established a machine learning framework known as chemical reaction neural networks (CRNNs). By incorporating the fundamental physical laws such as the law of mass action and the Arrhenius law into the structure of the neural networks, CRNNs offer a physically interpretable approach, capable of elucidating reaction pathways and kinetic parameters. Using the CRNN-based method, the kinetic parameters of biomass pyrolysis<sup>25</sup> and NCM cathode decomposition process<sup>26</sup> were revealed. These findings demonstrate the potential of CRNN methods in TR modeling, showcasing its applicability in elucidating complex reaction kinetics.

Motivated by the above considerations, the objectives of the present study are two-fold: (1) to construct a first-ever LIB TR gas generation chemical kinetic mechanism and (2) to enhance chemical insights by comparing the discovered pathways and chemical kinetic parameters with existing literature. Specifically, TR experiments for commercial 18650-type NCM cells with different initial SOCs, spanning from undercharged to overcharged states, are conducted to establish a training dataset. Employing an additional non-linear neural network to predict the mean molar weight of the generated gas, the CRNN models train a chemical kinetic mechanism with 7 species and 16 reactions, which can accurately predict the key parameters during the TR process. Furthermore, the CRNN models provide comprehensive elucidation of reaction pathways, demonstrating robust alignment with existing literature.

## RESULTS

### Experiment results

The evolution of surface temperature and inside-jar pressure for cells with different SOCs is plotted in Figure 1.<sup>34</sup> Consistent with the findings of Feng et al.,<sup>6</sup> three key thermal characteristic

temperatures,  $\{T_1, T_2, T_3\}$ , are readily observed to describe the TR processes for all cells. Specifically,  $T_1$  is the onset temperature for the self-heating of the cell,  $T_2$  is the separator collapsing temperature, and  $T_3$  is the maximum temperature. Note that  $T_1$  monotonically increases from 353 to 377 K with SOC decreasing from 120% to 50%. This is reasonable as  $T_1$  is controlled by the SEI decomposition from the anode.<sup>27</sup> A decreased SOC results in an increase in cell thermal stability, and thus increases  $T_1$ . During a long self-heating period of  $\sim \mathcal{O}(1,000)$  min, the cell temperature gradually increases and finally reaches  $T_2$ , in which the violent heat release stage of TR is initiated.<sup>3</sup> Similar to  $T_1$ ,  $T_2$  is generally higher for cells with lower SOCs. After the temperature reaches  $T_2$ , a large amount of heat is generated within a few seconds, leading the cell to reach  $T_3$ . Note that  $T_3$  is decreased with decreased SOC, indicating that the corresponding cell is less reactive with suppressed exothermic reactions.

On the other hand, the pressure experiences a smooth increase before the temperature reaches  $T_2$ , suggesting less amount of gas is generated before  $T_2$ .

Note that this pressure increase is primarily attributed to two factors, namely electrolyte evaporation and gas generation from side reactions. The contributions of these two factors to the pressure increase are illustrated in Figure S1. However, after  $T_2$ , the pressure rapidly increases to its peak magnitude,  $P_3$ . Moreover, the variations for  $P_3$  between cells with different SOCs are much more obvious than those of  $T_3$ , indicating that the total amount of released gas greatly differs for batteries with various SOCs.

With the above temperature and pressure data, the battery venting gas (BVG) amount is obtained by applying the ideal gas equation.<sup>9,10,22</sup> These experimental results of batteries with various SOCs are adopted as the database for the current study. Three sets of data with SOC of 120%, 100%, and 50%, covering a range from undercharged to overcharged conditions,

**Table 1. Learned LIB TR gas generation reaction pathways interpreted from CRNN**

No.	Reaction	$E_a$ (kJ/mol)	b	In A
<b>(a) Learned pathways for the self-heating process</b>				
R1	$0.107 \text{ Li}^+ + 0.083 \text{ LIB} \rightarrow 0.045 \text{ S}_2 + 0.010 \text{ S}_5 + 0.023 \text{ BVG}$	66.261	0.115	6.887
R2	$0.136 \text{ Li}^+ + 0.119 \text{ LIB} \rightarrow 0.078 \text{ S}_2 + 0.010 \text{ S}_3 + 0.010 \text{ S}_4 + 0.020 \text{ BVG}$	63.782	0.149	7.012
R3	$0.095 \text{ Li}^+ + 0.010 \text{ LIB} + 0.012 \text{ S}_3 + 0.015 \text{ S}_4 + 0.019 \text{ S}_5 \rightarrow 0.033 \text{ S}_2 + 0.023 \text{ BVG}$	63.432	0.145	6.933
R4	$0.095 \text{ Li}^+ + 0.012 \text{ LIB} + 0.012 \text{ S}_3 + 0.010 \text{ S}_4 + 0.010 \text{ S}_5 \rightarrow 0.018 \text{ S}_2 + 0.019 \text{ BVG}$	67.211	0.106	6.741
R5	$0.110 \text{ Li}^+ + 0.019 \text{ S}_3 + 0.013 \text{ S}_4 + 0.010 \text{ S}_5 \rightarrow 0.017 \text{ S}_2 + 0.020 \text{ BVG}$	65.230	0.142	6.904
R6	$0.103 \text{ Li}^+ + 0.024 \text{ LIB} + 0.019 \text{ S}_3 + 0.013 \text{ S}_4 \rightarrow 0.023 \text{ S}_2 + 0.031 \text{ BVG}$	63.508	0.100	6.952
R7	$0.098 \text{ Li}^+ + 0.014 \text{ LIB} + 0.017 \text{ S}_3 + 0.013 \text{ S}_4 \rightarrow 0.011 \text{ S}_2 + 0.010 \text{ S}_5 + 0.023 \text{ BVG}$	66.846	0.119	6.644
R8	$0.126 \text{ Li}^+ + 0.030 \text{ LIB} + 0.021 \text{ S}_3 + 0.014 \text{ S}_4 \rightarrow 0.032 \text{ S}_2 + 0.038 \text{ BVG}$	60.876	0.142	6.911
<b>(b) Learned pathways for the violent TR process</b>				
R9	$0.146 \text{ Li}^+ + 0.117 \text{ LIB} \rightarrow 0.010 \text{ S}_4 + 0.112 \text{ BVG}$	47.591	0.191	5.828
R10	$0.122 \text{ Li}^+ + 0.093 \text{ LIB} \rightarrow 0.010 \text{ S}_4 + 0.088 \text{ BVG}$	48.255	0.150	5.532
R11	$0.111 \text{ Li}^+ + 0.013 \text{ S}_5 \rightarrow 0.013 \text{ S}_2$	49.966	0.101	5.322
R12	$0.119 \text{ Li}^+ + 0.011 \text{ S}_2 \rightarrow 0.011 \text{ S}_5$	50.362	0.089	5.381
R13	$0.106 \text{ Li}^+ + 0.013 \text{ S}_4 \rightarrow 0.011 \text{ S}_2$	50.826	0.082	5.237
R14	$0.140 \text{ Li}^+ + 0.047 \text{ LIB} + 0.019 \text{ S}_2 \rightarrow 0.012 \text{ S}_5 + 0.053 \text{ BVG}$	48.742	0.148	5.621
R15	$0.120 \text{ Li}^+ + 0.016 \text{ S}_2 \rightarrow 0.015 \text{ S}_4$	50.204	0.070	5.356
R16	$0.100 \text{ Li}^+ + 0.015 \text{ S}_2 \rightarrow 0.015 \text{ S}_5$	51.227	0.084	5.291

are selected as training datasets, while the data with SOC of 70% is selected as the test dataset.

### Kinetic model results

As a digital twin of the chemical reaction network, the weights and biases obtained in the CRNN model are physically interpretable.<sup>24,25</sup> As visualized in Figure S2, learned weights and biases can be categorized into stoichiometric coefficients of reactants and products, as well as Arrhenius parameters ( $E_a$ , b, and lnA). Moreover, in  $w_{out}$ , a negative stoichiometric coefficient represents a reactant, while a positive coefficient corresponds to a product. The above-mentioned neural network parameters are as such interpreted into learned reaction pathways, and the corresponding kinetic parameters of the LIB TR process are illustrated in Table 1. Seven species (Li<sup>+</sup>, LIB, BVG, and four other intermediate species, S2-S5) and 16 reactions (8 reactions for the self-heating process and 8 reactions for the violent TR process) are used, as justified in methods. Figure 2 then validates the predicted LIB TR gas generation amount with the experimental results. It is readily observed that, for the self-heating process, the proposed mechanism well predicts the key parameters, including the separator collapsing timing,  $T_2$ , and the corresponding gas generation amount,  $n_2$ , for all the cases with different SOCs. Note that, the accurate prediction of  $T_2$  and  $n_2$  is of importance in identifying the initial mass concentration vector,  $\hat{m}_2$ . Consequently, the predicted and measured maximum gas generation amount,  $n_3$ , during the violent TR process also shows good agreement, indicating the proposed CRNN derives accurate reaction schemes.

The chemical interpretation of the derived reaction pathways also agrees well with the current literature. The main insights revealed by the CRNN are listed below.

- (1) The active components within LIB initially consume Li<sup>+</sup> to primarily produce S<sub>2</sub> and BVG through R2 and R8. These reactions likely represent the initial decomposition phase of the SEI layer. The SEI decomposition reaction is typically regarded as the first side reaction during the full TR process. Assume that the main component of the SEI is (CH<sub>2</sub>OCO<sub>2</sub>Li)<sub>2</sub>, R2 and R8 could yield gas components such as CO<sub>2</sub> and C<sub>2</sub>H<sub>4</sub>, alongside solid residues such as Li<sub>2</sub>CO<sub>3</sub>.<sup>27</sup>
- (2) After the SEI layer breakdown, the exposed anode might react with the electrolyte, resulting in the generation of C<sub>2</sub>H<sub>4</sub> and C<sub>2</sub>H<sub>6</sub>.<sup>28</sup> As the temperature further increases, the electrolyte can evaporate into vapor, such as diethyl carbonate (DEC), ethyl methyl carbonate (EMC), and ethylene carbonate (EC). Meanwhile, the NCM cathode can directly decompose to release O<sub>2</sub>.<sup>29</sup> O<sub>2</sub>, as an oxidant, further accelerates the side reactions between the cathode and the electrolyte vapor.<sup>4</sup> For these complex interactions, the corresponding reaction pathways can be explained by R1, R3-R7.
- (3) According to the reaction rate coefficients, the activation energies for the violent TR process reactions are generally lower than those of the self-heating process reactions. This suggests that the energy barrier for these reactions is smaller, allowing reactant molecules to more easily collide with sufficient energy to overcome it. As a result, the violent TR process reactions proceed at a faster rate, which aligns with the findings of Wang et al.<sup>3</sup>
- (4) Following the separator failure, direct contact between the anode and cathode materials could form an internal short circuit (ISC).<sup>30</sup> The electric energy stored within the battery releases and triggers the violent TR. In a recent study by Feng et al.,<sup>31</sup> in the absence of ISC, the chemical crosstalk between the active components instigates the

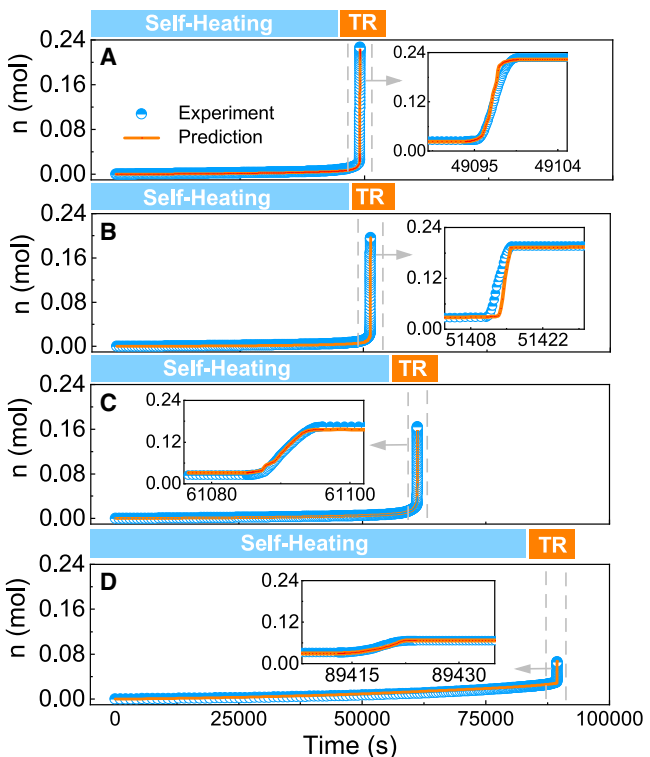


**Figure 2.** Predicted gas generation amount (lines) and the corresponding experimental results (symbols) for NCM TR processes with different SOCs

- (A) Predicted and experimental gas generation amounts at 120% SOC.
- (B) Predicted and experimental gas generation amounts at 100% SOC.
- (C) Predicted and experimental gas generation amounts at 70% SOC.
- (D) Predicted and experimental gas generation amounts at 50% SOC.

violent TR. Even without gas generation,<sup>32</sup> these reactions are important in triggering TR and can be represented by R11-R13 and R15-R16.

- (5) At higher temperatures, the electrolyte itself undergoes pyrolysis or oxidation with the O<sub>2</sub> or other active materials released from the cathode decomposition.<sup>18</sup> These reactions are widely recognized as the main contributor to the gas generation.<sup>33</sup> As shown in Table 1, R9, R10, and R14 are responsible for the gas generation from electrolyte decomposition.

In addition, the chemical kinetic parameters in Table 1 are validated against those in the literature. In a recent experimental study, Mao et al.<sup>22</sup> conducted TR experiments on 18650-type LIBs with a cathode material consisting of 98% LiNi<sub>0.5</sub>Co<sub>0.2</sub>Mn<sub>0.3</sub>O<sub>2</sub> and 2% LiMn<sub>2</sub>O<sub>4</sub>. Two sets of kinetic parameters were employed to describe the gas generation dynamic of the self-heating process and the violent TR process, respectively. Figure 3 compares the determined rate constants in this study with those in Mao et al.<sup>22</sup> As for the self-heating process (see Figure 3A), R2, R3, and R8 with higher rate constants are the dominant reactions for the BVG accumulation. The rate constants of these reactions align well with that proposed by Mao et al.<sup>22</sup> Note that, instead of being represented by a single reaction, the

newly developed kinetic parameters can separately describe multiple reactions, including SEI decomposition, cathode material decomposition, and the interaction between the cathode and electrolyte, as previously stated. On the other hand, as evident in Figure 3B, R9 serves as the primary gas generation reaction during the violent TR process, followed by R10 and R14. The rate constants of these reactions are comparable with that in Mao et al.,<sup>22</sup> indicating the accuracy of the autonomously explored gas generation dynamic parameters. Note that, other reactions without BVG generation (R11-R13 and R15-16) are employed to describe the TR process. This kinetic mechanism, compared with assuming a one-step reaction scheme, is thus more realistic because it also considers reactions between cathode and anode materials that do not directly generate gas but are still important in triggering the violent TR.

To better understand the proposed chemical kinetics, Figure 4 depicted the species evolution of the LIB TR process for battery with an initial SOC of 100%. It is readily observed that S<sub>2</sub> and BVG gradually accumulate during the self-heating process (see Figure 4A). Based on the reaction pathways depicted in Table 1 and the reaction rate compared in Figure 3, BVG is primarily generated through R2, R3, and R8, while S<sub>2</sub> is produced through the interactions between LIB, S<sub>3</sub>, and S<sub>4</sub>. Moreover, the generated S<sub>2</sub>, BVG, and the remaining LIB participate in the violent TR process (see Figure 4B), in which S<sub>2</sub> and LIB consume simultaneously to generate S<sub>4</sub>, S<sub>5</sub>, and BVG by R9-R16. Similar species profile trends are observed for other cases with different initial SOCs. The corresponding profiles can be found in Figure S3. It is therefore concluded that the autonomously learned kinetic mechanism is suitable for predicting the LIB TR gas generation process, regardless of the initial SOCs.

## DISCUSSION

To further validate the applicability of the proposed mechanism, its ability to predict the TR gas generation process for cells with varied capacities and cathode materials is tested. Specifically, a dataset including the temperature and pressure profiles during TR of a 26700-type (26 mm in diameter and 70 mm in length) LiNi<sub>0.5</sub>Co<sub>0.2</sub>Mn<sub>0.3</sub>O<sub>2</sub> (NCM523) cell with a capacity of 5,000 mAh is selected from Jia et al.<sup>16</sup> Similar to this work, the top cap of the cell is removed, allowing full-cycle TR process pressure detection. To mimic the larger active material contents inside the 5,000 mAh NCM523 cell, the embedded lithium ions (Li<sup>+</sup>) amount is increased from 3 to 5. The TR gas generation reaction pathways and chemical kinetic parameters, as listed in Table 1, are employed to predict the gas generation amount and corresponding pressure during the TR process.

The pressure predicted by the learned CRNN kinetic mechanism is compared with that of the experimental data, as illustrated in Figure 5. It is readily observed that the proposed mechanism well predicted the pressure trace during the self-heating process. Moreover, the predicted maximum pressure of TR, P<sub>max</sub>, is nearly identical to that of the experimental data. This is reasonable as the effects of the enlarged embedded lithium ions content and cell capacity are considered in the simulation. However, during the violent TR, the proposed mechanism predicts a generally smoother

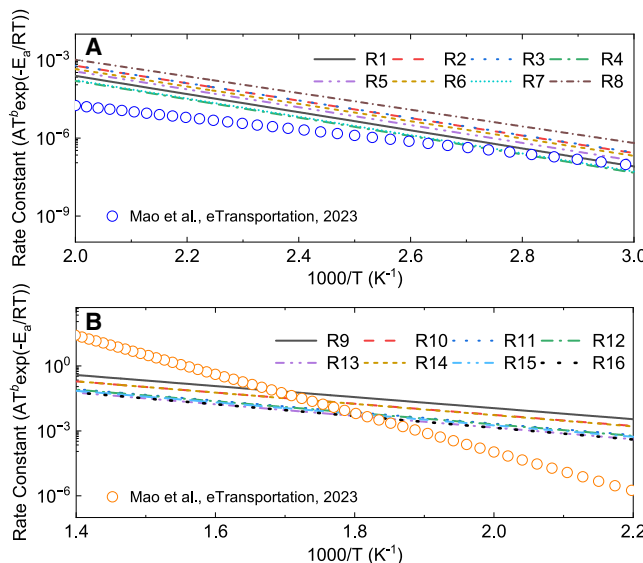


**Figure 3. Comparisons of the discovered rate constants for the TR gas generation process with the state-of-the-art results by Mao et al.<sup>22</sup>**

(A) Comparisons of rate constants during the self-heating process.  
(B) Comparisons of rate constants during the violent TR process.

reaction process, indicated by the longer time to reach  $P_{\max}$  from  $P_{SC}$ . This is because the current CRNN model is trained using the database of NCM111 cells. As the cathode material varies from NCM111 to NCM532, the higher nickel content could lead to a more severe and quicker TR process.

To summarize, the CRNN-based model proposed in this study shows great potential to predict the TR gas generation process. Given the training dataset, the kinetic parameters developed in this study are primarily applicable to 18650-type NCM111 cells. To further enhance the applicability of the kinetic mechanism beyond 18650-type NCM111 cells, incorporating more experimental data into the CRNN training process is essential for capturing reaction kinetics across cells with different capacities and cathode materials.

## METHODS

### Experimental methods

The LIB cells tested in this study were commercial NCM batteries (Shenzhen Doublepow Technology, China), with a diameter of 18 mm, a length of 65 mm, and a capacity of 2,500 mAh. The cathode and anode materials were  $\text{LiNi}_{1/3}\text{Co}_{1/3}\text{Mn}_{1/3}\text{O}_2$  (NCM 111) and natural graphite, respectively. The electrolyte primarily consisted of DEC, EMC, and EC, with the salts of  $\text{LiPF}_6$ . Four SOCs were selected in this study, namely 120%, 100%, 70%, and 50%, respectively. Note that the cells were charged and discharged three times to rate their capacity and then recharged to the desired SOCs by setting the ratio between the charged capacity and the rated capacity.

The experimental setup is consistent with that described in the prior study.<sup>34</sup> Specifically, an accelerating rate calorimeter (ARC, Hangzhou Young Instruction Science & Technology, China) was

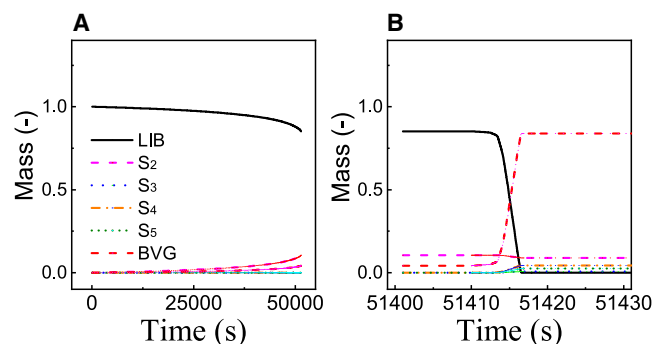


**Figure 4. Species profiles for LIB TR process with a SOC of 100% using the learned kinetic mechanism**

(A) Species profiles with 100% SOC during the self-heating process.  
(B) Species profiles with 100% SOC during the violent TR process.

employed to measure the TR behavior of cells with different SOCs. The ARC operated in the heat-wait-seek mode<sup>9,10</sup> to accurately capture the onset temperature of TR and guarantee a uniform equilibrium quasi-adiabatic state during the TR process. Before the TR test, the top cap and safety valve of the cell were removed inside a nitrogen-filled glove box to allow for the measurement of internal pressure during the self-heating process before gas venting. The cells were then put inside a stainless airtight jar within the ARC to facilitate the measurement of gas generation characteristics throughout the TR process. The stainless airtight jar has an inner radius of 39 mm and a height of 68 mm, which allows a maximum pressure of 20 MPa. As the main gas generation process of TR is generally rapid,<sup>22</sup> the pressure transducer was set to detect the inner pressure of the jar with a high frequency of 1,000 Hz. Moreover, a battery testing system (CT-4008-5V20A-A, Shenzhen Neware Technology, China) and a gas chromatograph (GC, Agilent 7890B) were employed for the detection of the corresponding electrochemical and gas-generated properties of the cell during the TR process, respectively. Note that, to guarantee the reliability and accuracy of the experimental data, the cell TR tests for each SOC level were performed multiple times, with at least three repetitions to facilitate cross-validation. A detailed comparison of the different tests is shown in Figure S4. For more details, the readers are referred to our previous studies.<sup>23,34</sup>

### CRNN method

The CRNN has been developed by Deng and co-workers<sup>24,25</sup> to autonomously discover unknown reaction pathways from the evolution profiles of chemical species. In this section, a brief overview of the CRNN model will be provided, integrating specific constraints related to LIB TR gas generation process into the framework. Specifically, the proposed CRNN models describe a system comprising: (1) the active materials within the battery as the reactant, donated by LIB, (2)  $n - 1$  intermediate species, namely  $[S_2, S_3, \dots, S_n]$ , along with (3) the battery venting gas, BVG, as the products. Note that, in this study, the battery SOC status is represented by the embedded lithium ion,  $\text{Li}^+$ , within the anode ( $\text{Li}_x \text{C}_6$ ).<sup>8,35</sup>

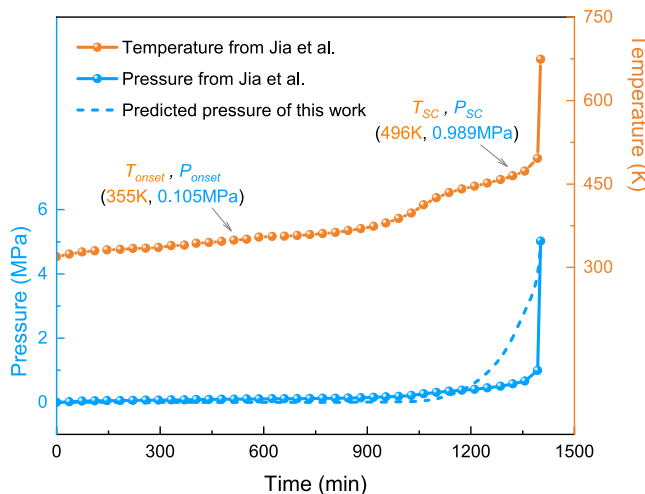
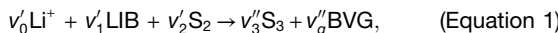


**Figure 5.** Comparison of the predicted pressure by the learned kinetic mechanism and the tested pressure<sup>16</sup> of a 26700-type NCM523 cell with a capacity of 5,000 mAh during TR

As an illustrative example, the following reaction,  $R_i$ , from the entire kinetic mechanism is considered:



where  $v'_i$  and  $v''_i$  represent the stoichiometric coefficients of the reactants and products, respectively. Assuming that the reaction orders are equivalent to the stoichiometric coefficients, the reaction rate can be determined by three parameters, namely the pre-factor  $A$ , non-exponential temperature dependence factor  $b$ , and the activation energy  $E_a$ . By utilizing the law of mass action and Arrhenius law, the reaction rate equation is formulated and subsequently rearranged in the following manner:

$$\begin{aligned} r &= [\text{Li}^+]^{v'_0} [\text{LIB}]^{v'_1} [\text{S}_2]^{v'_2} A T^b \exp(-E_a/RT) \\ &= \exp(v'_0 \ln[\text{Li}^+] + v'_1 \ln[\text{LIB}] + v'_2 \ln[\text{S}_2] \\ &\quad + \ln A + b \ln T - E_a/RT). \end{aligned} \quad (\text{Equation 2})$$

Subsequently, the production rate of each species in [Equation 1](#) can be written as:

$$\frac{d[\text{LIB}]}{dt} = [\dot{\text{LIB}}] = -v'_1 r \quad (\text{Equation 3})$$

$$\frac{d[\text{S}_2]}{dt} = [\dot{\text{S}}_2] = -v'_2 r$$

$$\frac{d[\text{S}_3]}{dt} = [\dot{\text{S}}_3] = v''_3 r$$

$$\frac{d[\text{BVG}]}{dt} = [\dot{\text{BVG}}] = v''_g r.$$

In this study, a single neuron within the neural network is employed to identify the optimal solution of  $v'_i$ ,  $v''_i$ , and  $r$ , thereby determining the corresponding production rates. For this single neuron, its expression can be written as,

$$\begin{aligned} y &= \sigma(\mathbf{wx} + b) \\ &= \exp([v_0 \ v_1 \ \dots \ v_n \ b \ E_a] \\ &\quad \times [\ln[\text{Li}^+] \ \ln[\text{LIB}] \ \dots \ \ln[\text{S}_n] \ \ln T \ - 1/RT]^T + \ln A) \end{aligned} \quad (\text{Equation 4})$$

where  $\mathbf{y}$  is the output,  $\mathbf{x}$  represents the input,  $\mathbf{w}$  denotes the weights, and  $\sigma(\cdot)$  is the non-linear activation function. As illustrated in the blue box of [Figure 6](#), the detailed definitions of these parameters are based on [Equation 2](#). Specifically, the exponential function  $\exp(\cdot)$ , is employed as the activation function, introducing non-linearity into the model and enabling the network to capture more complex patterns inherent to the reaction dynamics. The inputs,  $\mathbf{x}$ , are the logarithmic concentrations of all species and the corresponding temperature at current time step. The production rates of these species at the subsequent time step serve as the outputs,  $\mathbf{y}$ . Moreover, the input layer weights,  $\mathbf{w}_{\text{in}}$ , represent the reaction order as well as the Arrhenius parameters  $b$  and  $E_a$ , while the bias corresponds to the pre-exponential factor  $A$  on the logarithmic scale. Consequently, the output weights  $\mathbf{w}_{\text{out}}$  correspond to the stoichiometric coefficients.

As shown in the pink box of [Figure 6](#), considering that the LIB TR gas generation process involves multiple reactions, the same amount of neurons are stacked to form a neural network, facilitating the discovery of potential unknown reaction pathways. Note that the TR experiments conducted in this study quantify only the molar value of BVG, released over a specific unit of time. To predict the corresponding mass of BVG, its mean molar weight,  $\bar{M}$ , is involved in the CRNN framework implemented by an extra non-linear molar value network (MVN) module, as shown in the yellow box of [Figure 6](#). Here, another neural network is employed for modeling, which integrates the predicted mass output from the CRNN ( $\hat{\mathbf{m}}(t)$ ) and a matrix comprising  $T$ ,  $P$ , and  $[\text{Li}^+]$  as inputs to predict  $\bar{M}$ . As stated in Koch et al.<sup>11</sup> and Golubkov et al.,<sup>36</sup> the primary components of BVG are the evaporated electrolytes,  $\text{H}_2$ ,  $\text{CH}_4$ ,  $\text{CO}$ ,  $\text{CO}_2$ ,  $\text{C}_2\text{H}_4$ , and  $\text{C}_2\text{H}_6$ , and vary along with time. Therefore,  $\bar{M}$  is constrained within the range of (12,44) g/mol, expressed as:

$$\bar{M} = 28 + 16 \cdot \sigma(\mathbf{XW}_{\bar{M}} + \mathbf{b}_{\bar{M}}) \quad (\text{Equation 5})$$

$$\mathbf{X} = \text{LayerNorm}([\hat{\mathbf{m}}(t), T, P, \text{Li}^+]),$$

where  $\hat{\mathbf{m}}(t)$  is the predicted mass output from the CRNN model,  $\mathbf{W}_{\bar{M}}$  and  $\mathbf{b}_{\bar{M}}$  are the weight matrices and the bias vectors for the network, respectively. LayerNorm<sup>37</sup> is a normalizer used to improve stability, speed up training, and reduce the effects of internal covariate shifts in models. The hyperbolic tangent function  $\tanh(\cdot)$  is used as the activation function

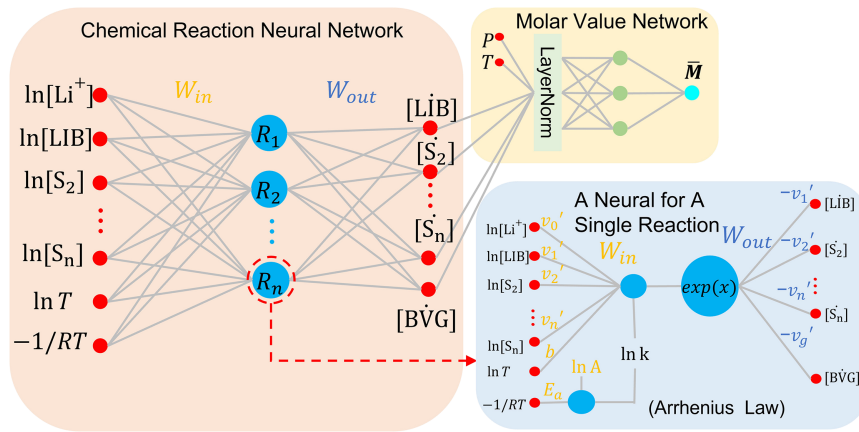


**Figure 6.** Schematic of the LIB TR gas generation kinetic mechanism modeling approach

The left part is CRNN architecture for multi-step reactions involves stacking neurons into a hidden layer. The right part is the mean molar mass predictor involves a non-linear neural network (up) and a neuron for a single reaction (down).

$\sigma(\cdot)$ . It converts the input to a range between  $-1$  and  $1$ , centering the output around zero, leading to more efficient weight updates and faster convergence.

As for the inference process of the reaction network, the CRNN is trained using experimental data. Since the vector of species concentration  $\mathbf{Y}$  evolves with time, the aim is to discover a CRNN that satisfies the observed dynamics of  $\dot{\mathbf{Y}}$  while incorporating the constraints mentioned earlier as

$$\dot{\mathbf{Y}} = \text{CRNN}(\mathbf{Y}). \quad (\text{Equation 6})$$

To obtain predictions for the mass loss of LIB, an ODE system can be formulated using [Equation 6](#) and solved numerically in an ordinary differential equation (ODE) integrator as

$$\widehat{\mathbf{m}}(t) = \text{ODESolve}(\text{CRNN}(\mathbf{Y}), \mathbf{Y}_0; T_0, [\text{Li}^+]), \quad (\text{Equation 7})$$

where  $\mathbf{Y}_0$  is a vector containing the initial concentrations,  $T_0$  is the initial temperature, and  $[\text{Li}^+]$  represents concentrations of active lithium within the cathode. The resulting solution, denoted as  $\widehat{\mathbf{m}}(t)$ , yields a vector of all species concentrations at each time step.

To optimize the CRNN model parameters, a loss function is defined to quantify the difference between the measured and predicted time series of mass loss,  $\widehat{\mathbf{m}}(t)$ . To be specific,  $\widehat{\mathbf{m}}(t)$  can be classified into the mass of solid residuals  $\widehat{\mathbf{m}}_{\text{res}}$  and mass of venting gas  $\widehat{\mathbf{m}}_{\text{gas}}$ . Assuming the initial mass is  $\mathbf{m}_0$ , then the mean absolute error (MAE) is adopted as the loss metric as:

$$\begin{aligned} \text{Loss} = & \text{MAE}(\mathbf{m}_{\text{gas}}, \widehat{\mathbf{m}}_{\text{gas}}) + \text{MAE}(\mathbf{m}_{\text{res}}, \widehat{\mathbf{m}}_{\text{res}}) \\ & + \text{MAE}(\widehat{\mathbf{m}}(t), \mathbf{m}_0), \end{aligned} \quad (\text{Equation 8})$$

where the first term quantifies the discrepancy between the measured and predicted gas mass residuals of BVG. The second term evaluates the difference between the solid residual mass predicted by the CRNN model ( $\widehat{\mathbf{m}}_{\text{res}}$ ) and the dataset. Note that, to facilitate the logarithmic operation presented in [Equation 2](#), it is necessary to constrain the mass fraction to a non-negative value. To achieve this, a simple clipping mech-

anism is employed as in Ji et al.,<sup>25</sup> where the mass fraction,  $\mathbf{Y}$ , is set to  $\max(\text{eps}, \mathbf{Y})$ , with  $\text{eps} = 1e-8$  being used consistently throughout our work. This clipping mechanism may introduce a slight imbalance in the total mass. To avoid this, the third term of [Equation 8](#) is incorporated to stabilize the ODE solver. This term is primarily effective during the early stages of prediction, where it prevents the occurrence of negative values in the initial epochs. As the optimization progresses and mass conservation becomes strictly maintained, the value of this term naturally converges to zero, ensuring no interference with the final optimization. The absolute tolerance of the ODE solver is also set to  $\text{eps}$ , which ensures good numerical stability without sacrificing time complexity. The differential programming package `torchdiffeq`<sup>38</sup> has been instrumental in efficiently computing gradients concerning CRNN parameters by enabling differentiation across the ODE integrators. Leveraging the interpolation-based adjoint method during the backward call facilitates gradient computation. Subsequently, the optimization process employs the Adam optimizer<sup>39</sup> as our stochastic gradient descent method to learn the CRNN parameters.

As readily observed in [Figure 1](#), the LIB TR process can be divided into two stages, namely the self-heating stage and the violent TR process, employing the characteristic temperature matrix  $\{T_1, T_2, T_3\}$ . The self-heating process is typically smooth with a slight temperature increase with  $\sim \mathcal{O}(1,000)$  min, while the violent TR process could occur within a few seconds.<sup>3,6</sup> To maintain the integrity of the system and reduce its overall stiffness, two CRNN models are connected to separately learn the self-heating process and the violent TR process. Two training approaches are considered, namely the sequential training approach and the joint training approach. The sequential training approach first trains the self-heating process, followed by the violent TR process. While this approach may yield two locally optimal models, it does not guarantee an optimal solution for the overall process. In contrast, the joint training approach simultaneously trained both processes with shared parameter settings, as illustrated in [Figure 7](#). At the beginning of each epoch, the species concentration vector,  $\mathbf{Y}$ , is passed to the CRNN for the self-heating process. This CRNN predicts  $\dot{\mathbf{Y}}$  using the ODE solver. Upon completion of the self-heating process, a matrix composed of  $\mathbf{Y}$  at each time step is generated. The final  $\mathbf{Y}$  of this process is then transferred to the CRNN for the violent TR process, predicting  $\dot{\mathbf{Y}}$  and generating the corresponding

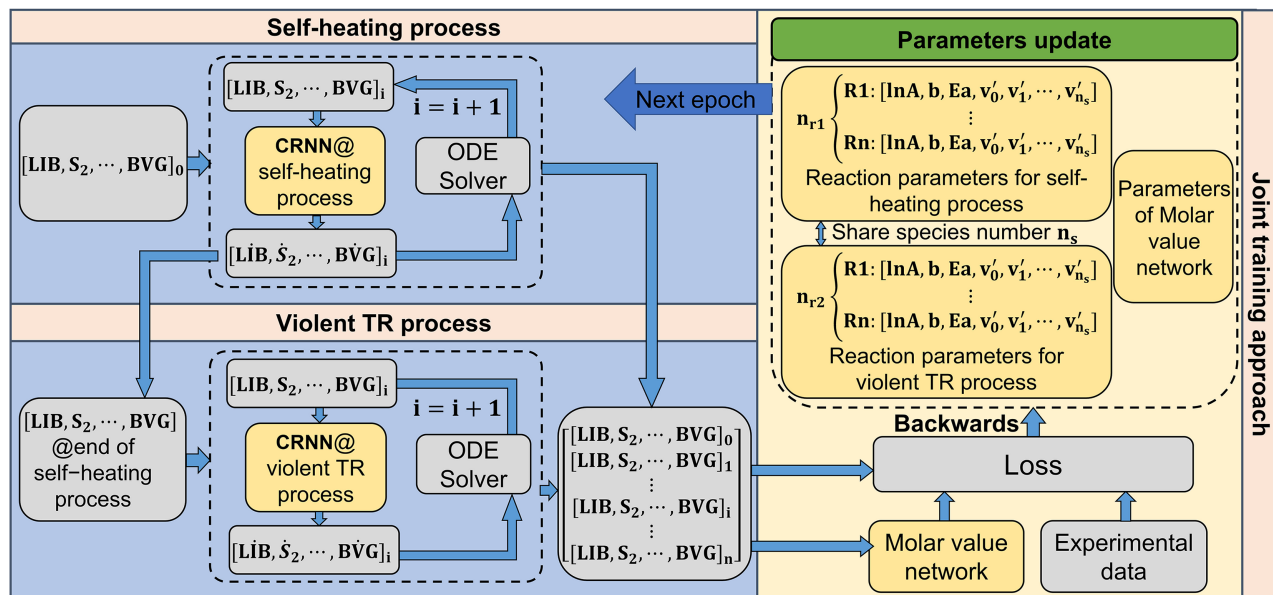


**Figure 7. Flowchart of the joint training approach**

matrix of  $\mathbf{Y}$  for this stage. These two concentration matrices are combined with the MVN network and compared against experimental data to calculate the loss function. Backpropagation is employed to optimize the kinetic parameters of all three networks, repeating across epochs to progressively minimize the loss until the network converges. As the loss function integrates the losses from both processes as a whole, this parallel training strategy enhances the ability of the model to capture dependencies and synergies between the two processes, minimizes error propagation, and results in a more coherent, efficient system that achieves a globally optimal solution. Therefore, the joint training approach is selected in the following study.

### Training strategies

#### Species and reaction numbers

The number of species and reactions is treated as hyperparameters for the CRNN model (the orange box of Figure 6), which correspond to the number of nodes in the output layer and hidden layer, respectively. In this work, a grid search method is employed to determine these two hyperparameters by increasing the proposed number of species and reactions until the model fitness can no longer be improved. Note that the number of species in the self-heating and violent TR processes should be strictly consistent to comply with the consistency of the reaction. Therefore, the number of species for both the self-heating and violent TR processes is first selected, followed by a grid search to optimize the number of reactions for each process. This procedure is repeated for different species configurations until the combination with the lowest test loss value is selected. The dependence of minimum loss functions for the test datasets on the number of proposed species and reactions of self-heating process and violent TR processes is depicted in Figure 8. It is readily

observed that the global average loss for the two processes is minimized (0.092) when the number of species is set to seven. Consequently, seven is selected as the optimal number of species. Under this configuration, different reaction number combinations corresponding to the minimum loss value are chosen for the self-heating and violent TR processes, respectively. The results show that eight reactions for the self-heating process and an additional eight reactions for the violent TR process achieve optimal fitting performance, as highlighted by the red circle. Note that this configuration also provides the best fitting performance for the BVG gas prediction (the first term of Equation 8) and the residual mass prediction (the second term of Equation 8). For further details, readers are referred to Figure S5.

#### Learning rate and gradient clipping

The same training strategy is applied for both the self-heating and violent TR processes, using learning rate annealing to fine-tune the model. The initial learning rate is set to 5e-4, and decreases by a factor of 0.2 every 500 epochs until reaching a minimum value of 1e-5. In addition, gradient clipping with a threshold of 1e-2 is used to avoid gradient explosion when solving the ODE. Correspondingly, the maximum step size of the ODE solver is restricted to the distance between two adjacent data points to ensure solver stability. Each process is trained for at least 2,000 epochs, with each epoch involving parameter updates under different experimental conditions. To stabilize the training process and reduce overfitting, regularization techniques are incorporated into the training process. Specifically, L2 regularization is added to the loss function, and mean-variance normalization is applied at the input layer. These settings facilitate a more robust and generalizable solution. Moreover, to ensure the stability of the ODE solution process, the MVN module is not updated during the first 300 epochs, minimizing its impact on the other

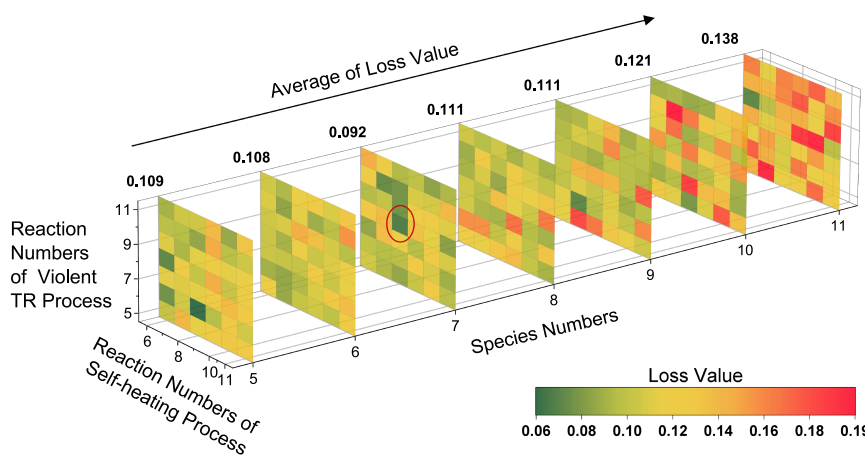


**Figure 8.** Heatmap of the dependence of minimum loss functions for the test data-sets on the number of proposed species and reactions

variables as much as possible. During the training process, if both test and train losses exhibit a continuous increase, the flexibility of MVN allows for the training to be early stopped. By adjusting the MVN structure, the training can proceed more effectively. Figure 9 shows the evolution of the loss function value during the CRNN training process using the finest species and reaction numbers obtained in Figure 8. As seen in Figure 9, the loss function value gradually converges after around 600 epochs. Note that, due to the distribution differences between the training and test sets, slight fluctuations in test loss can still be observed around 600 epochs. However, stopping training at the point of minimum test loss does not necessarily ensure a globally optimal solution. Refining the MVN structure and continuing training beyond this point further optimizes the model performance on the training set, achieving a better balance between the training and test sets. Therefore, these fluctuations do not indicate instability but rather reflect the ongoing optimization process of the model. After keeping the training process for another 200 epochs, the loss function value stops decreasing at a relatively low magnitude 0.08. With a test loss as low as 0.08, indicating that the training is not overfitted. By comprehensively considering the loss of both the training set and the test set, the optimal model is selected to obtain the final kinetic parameters.

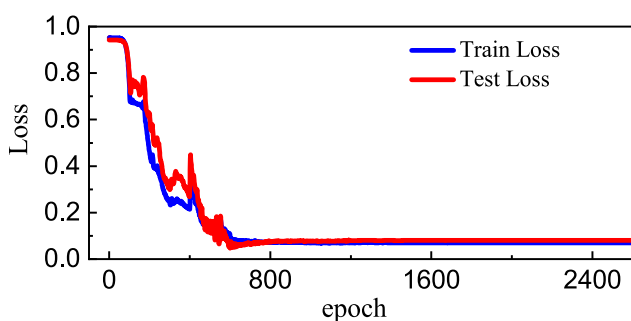


**Figure 9.** The loss value during the LIB TR process with the number of epochs

## RESOURCE AVAILABILITY

### Lead contact

Further information and requests for resources and reagents should be directed to and will be fulfilled by the lead contact, Jiabo Zhang ([zhangjiabo@sjtu.edu.cn](mailto:zhangjiabo@sjtu.edu.cn)).

### Materials availability

This study did not generate new unique materials.

### Data and code availability

A repository containing the data and codes for reproducing this work is available at <https://github.com/348396272/CRNN-for-battery-thermal-runaway>. If you have any additional questions, please reach out to the [lead contact](#) for assistance.

## ACKNOWLEDGMENTS

This research work is supported by the National Natural Science Foundation of China (grant No. 52106261) and the Shanghai Pujiang Program (grant No. 24PJ058).

## AUTHOR CONTRIBUTIONS

Conceptualization, J.Z. and C.M.; methodology, J.Z. and P.H.; investigation, J.Z.; formal analysis, J.Z. and Q.G.; data curation, J.Z.; funding acquisition, J.Z., Z.H., and D.H.; writing – original draft, J.Z. and C.M.; writing – review & editing, D.H.; software, C.M., Shuaiqi Liu, and P.H.; validation, C.M. and Shuaiqi Liu; performance of parts of the experiments, Q.Z. and Shaoyan Liu; visualization, Shaoyan Liu; supervision and resources, Z.H.

## DECLARATION OF INTERESTS

The authors declare no competing interests.

## SUPPLEMENTAL INFORMATION

Supplemental information can be found online at <https://doi.org/10.1016/j.xcrp.2025.102563>.

Received: June 16, 2024

Revised: January 25, 2025

Accepted: April 7, 2025

Published: April 29, 2025

## REFERENCES

1. Zhang, X., Li, Z., Luo, L., Fan, Y., and Du, Z. (2022). A review on thermal management of lithium-ion batteries for electric vehicles. *Energy* 238, 121652. <https://doi.org/10.1016/j.energy.2021.121652>.
2. He, W., Guo, W., Wu, H., Lin, L., Liu, Q., Han, X., Xie, Q., Liu, P., Zheng, H., Wang, L., et al. (2021). Challenges and recent advances in high capacity li-rich cathode materials for high energy density lithium-ion batteries. *Adv. Mater.* 33, 2005937. <https://doi.org/10.1002/adma.202005937>.
3. Wang, Q., Mao, B., Stoliarov, S.I., and Sun, J. (2019). A review of lithium ion battery failure mechanisms and fire prevention strategies. *Prog. Energy Combust. Sci.* 73, 95–131. <https://doi.org/10.1016/j.pecs.2019.03.002>.
4. Feng, X., Ouyang, M., Liu, X., Lu, L., Xia, Y., and He, X. (2018). Thermal runaway mechanism of lithium ion battery for electric vehicles: A review. *Energy Stor. Mater.* 10, 246–267. <https://doi.org/10.1016/j.ensm.2017.05.013>.
5. Chen, Y., Kang, Y., Zhao, Y., Wang, L., Liu, J., Li, Y., Liang, Z., He, X., Li, X., Tavajohi, N., and Li, B. (2021). A review of lithium-ion battery safety concerns: The issues, strategies, and testing standards. *J. Energy Chem.* 59, 83–99. <https://doi.org/10.1016/j.jecchem.2020.10.017>.
6. Feng, X., Zheng, S., Ren, D., He, X., Wang, L., Cui, H., Liu, X., Jin, C., Zhang, F., Xu, C., et al. (2019). Investigating the thermal runaway mechanisms of lithium-ion batteries based on thermal analysis database. *Appl. Energy* 246, 53–64. <https://doi.org/10.1016/j.apenergy.2019.04.009>.
7. Duan, J., Tang, X., Dai, H., Yang, Y., Wu, W., Wei, X., and Huang, Y. (2019). Building safe lithium-ion batteries for electric vehicles: A review. *Electrochem. Energ. Rev.* 3, 1–42. <https://doi.org/10.1007/s41918-019-00060-4>.
8. Kim, Y. (2013). Mechanism of gas evolution from the cathode of lithium-ion batteries at the initial stage of high-temperature storage. *J. Mater. Sci.* 48, 8547–8551. <https://doi.org/10.1007/s10853-013-7673-2>.
9. Qin, P., Sun, J., and Wang, Q. (2021). A new method to explore thermal and venting behavior of lithium-ion battery thermal runaway. *J. Power Sources* 486, 229357.
10. Jia, Z., Wang, S., Qin, P., Li, C., Song, L., Cheng, Z., Jin, K., Sun, J., and Wang, Q. (2023). Comparative investigation of the thermal runaway and gas venting behaviors of large-format LiFePO<sub>4</sub> batteries caused by overcharging and overheating. *J. Energy Storage* 61, 106791. <https://doi.org/10.1016/j.est.2023.106791>.
11. Koch, S., Fill, A., and Birke, K.P. (2018). Comprehensive gas analysis on large scale automotive lithium-ion cells in thermal runaway. *J. Power Sources* 398, 106–112. <https://doi.org/10.1016/j.jpowsour.2018.07.051>.
12. Diaz, F., Wang, Y., Weyhe, R., and Friedrich, B. (2019). Gas generation measurement and evaluation during mechanical processing and thermal treatment of spent li-ion batteries. *Waste Manag.* 84, 102–111. <https://doi.org/10.1016/j.wasman.2018.11.029>.
13. Zhang, Y., Wang, H., Li, W., Li, C., and Ouyang, M. (2020). Quantitative analysis of eruption process of abused prismatic Ni-rich automotive batteries based on in-chamber pressure. *J. Energy Storage* 31, 101617. <https://doi.org/10.1016/j.est.2020.101617>.
14. Yuan, L., Dubaniewicz, T., Zlochower, I., Thomas, R., and Rayyan, N. (2020). Experimental study on thermal runaway and vented gases of lithium-ion cells. *Process Saf. Environ. Prot.* 144, 186–192. <https://doi.org/10.1016/j.psep.2020.07.028>.
15. Jin, Y., Zheng, Z., Wei, D., Jiang, X., Lu, H., Sun, L., Tao, F., Guo, D., Liu, Y., Gao, J., and Cui, Y. (2020). Detection of micro-scale Li dendrite via H<sub>2</sub> gas capture for early safety warning. *Joule* 4, 1714–1729. <https://doi.org/10.1016/j.joule.2020.05.016>.
16. Jia, Z., Qin, P., Li, Z., Wei, Z., Jin, K., Jiang, L., and Wang, Q. (2022). Analysis of gas release during the process of thermal runaway of lithium-ion batteries with three different cathode materials. *J. Energy Storage* 50, 104302. <https://doi.org/10.1016/j.est.2022.104302>.
17. Zhang, Q., Liu, T., Hao, C., Qu, Y., Niu, J., Wang, Q., and Chen, D. (2022). In situ Raman investigation on gas components and explosion risk of thermal runaway emission from lithium-ion battery. *J. Energy Storage* 56, 105905. <https://doi.org/10.1016/j.est.2022.105905>.
18. Zhang, J., Zhong, A., Huang, Z., and Han, D. (2022). Experimental and kinetic study on the stabilities and gas generation of typical electrolyte solvent components under oxygen-lean oxidation and pyrolysis conditions. *Sci. China Technol. Sci.* 65, 2883–2894.
19. Richard, M.N., and Dahn, J.R. (1999). Accelerating rate calorimetry study on the thermal stability of lithium intercalated graphite in electrolyte. i. Experimental. *J. Electrochem. Soc.* 146, 2068–2077. <https://doi.org/10.1149/1.1391893>.
20. Kim, G.-H., Pesaran, A., and Spotnitz, R. (2007). A three-dimensional thermal abuse model for lithium-ion cells. *J. Power Sources* 170, 476–489. <https://doi.org/10.1016/j.jpowsour.2007.04.018>.
21. Ren, D., Liu, X., Feng, X., Lu, L., Ouyang, M., Li, J., and He, X. (2018). Model-based thermal runaway prediction of lithium-ion batteries from kinetics analysis of cell components. *Appl. energy* 228, 633–644. <https://doi.org/10.1016/j.apenergy.2018.06.126>.
22. Mao, B., Fear, C., Chen, H., Zhou, H., Zhao, C., Mukherjee, P.P., Sun, J., and Wang, Q. (2023). Experimental and modeling investigation on the gas generation dynamics of lithium-ion batteries during thermal runaway. *eTransportation* 15, 100212.
23. Guo, Q., Liu, S., Zhang, J., Huang, Z., and Han, D. (2024). Effects of charging rates on heat and gas generation in lithium-ion battery thermal runaway triggered by high temperature coupled with overcharge. *J. Power Sources* 600, 234237. <https://doi.org/10.1016/j.jpowsour.2024.234237>.
24. Ji, W., and Deng, S. (2021). Autonomous discovery of unknown reaction pathways from data by chemical reaction neural network. *J. Phys. Chem. A* 125, 1082–1092. <https://doi.org/10.1021/acs.jpca.0c09316>.
25. Ji, W., Richter, F., Gollner, M.J., and Deng, S. (2022). Autonomous kinetic modeling of biomass pyrolysis using chemical reaction neural networks. *Combust. Flame* 240, 111992. <https://doi.org/10.1016/j.combustflame.2022.111992>.
26. Koenig, B.C., Zhao, P., and Deng, S. (2023). Accommodating physical reaction schemes in dsc cathode thermal stability analysis using chemical reaction neural networks. *J. Power Sources* 581, 233443. <https://doi.org/10.1016/j.jpowsour.2023.233443>.
27. Yang, H., Bang, H., Amine, K., and Prakash, J. (2005). Investigations of the exothermic reactions of natural graphite anode for Li-ion batteries during thermal runaway. *J. Electrochem. Soc.* 152, A73. <https://doi.org/10.1149/1.1836126>.
28. Yamaki, J., Takatsujii, H., Kawamura, T., and Egashira, M. (2002). Thermal stability of graphite anode with electrolyte in lithium-ion cells. *Solid State Ion.* 148, 241–245. [https://doi.org/10.1016/S0038-1826\(02\)00060-7](https://doi.org/10.1016/S0038-1826(02)00060-7).
29. Wang, H., Tang, A., and Huang, K. (2011). Oxygen evolution in overcharged Li<sub>x</sub>Ni<sub>1/3</sub>Co<sub>1/3</sub>Mn<sub>1/3</sub>O<sub>2</sub> electrode and its thermal analysis kinetics. *Chin. J. Chem.* 29, 1583–1588. <https://doi.org/10.1002/cjoc.2011080284>.
30. Feng, X., He, X., Ouyang, M., Lu, L., Wu, P., Kulp, C., and Prasser, S. (2015). Thermal runaway propagation model for designing a safer battery pack with 25 Ah LiNi<sub>x</sub>CoyMn<sub>z</sub>O<sub>2</sub> large format lithium ion battery. *Appl. energy* 154, 74–91. <https://doi.org/10.1016/j.apenergy.2015.04.118>.
31. Feng, X., Ren, D., He, X., and Ouyang, M. (2020). Mitigating thermal runaway of lithium-ion batteries. *Joule* 4, 743–770.
32. Mao, B., Chen, H., Cui, Z., Wu, T., and Wang, Q. (2018). Failure mechanism of the lithium ion battery during nail penetration. *Int. J. Heat Mass Transf.* 122, 1103–1115. <https://doi.org/10.1016/j.ijheatmasstransfer.2018.02.036>.
33. Harris, S.J., Timmons, A., and Pitz, W.J. (2009). A combustion chemistry analysis of carbonate solvents used in Li-ion batteries. *J. Power Sources* 193, 855–858. <https://doi.org/10.1016/j.jpowsour.2009.04.030>.
34. Zhang, J., Guo, Q., Liu, S., Zhou, C., Huang, Z., and Han, D. (2024). Investigation on gas generation and corresponding explosion characteristics of lithium-ion batteries during thermal runaway at different charge states. *J. Energy Storage* 80, 110201, URL. <https://doi.org/10.1016/j.est.2023.110201>.

110201. <https://www.sciencedirect.com/science/article/pii/S2352152X23036009>.
35. Manthiram, A. (2020). A reflection on lithium-ion battery cathode chemistry. *Nat. Commun.* 11, 1550. <https://doi.org/10.1038/s41467-020-15355-0>.
36. Golubkov, A.W., Scheikl, S., Planteu, R., Voitic, G., Wiltsche, H., Stangl, C., Fauler, G., Thaler, A., and Hacker, V. (2015). Thermal runaway of commercial 18650 Li-ion batteries with LFP and NCA cathodes – Impact of state of charge and overcharge. *RSC Adv.* 5, 57171–57186. <https://doi.org/10.1039/c5ra05897j>.
37. J. L. Ba, (2016) Layer normalization, arXiv Preprint at <https://doi.org/10.48550/arXiv.1607.06450>.
38. Chen, R.T.Q., Rubanova, Y., Bettencourt, J., and Duvenaud, D. (2018). Neural ordinary differential equations. In 32nd Conference on Neural Information Processing Systems (NeurIPS 2018). <https://doi.org/10.48550/arXiv.1806.07366>.
39. D. P. Kingma, J. Ba, Adam: A method for stochastic optimization, arXiv Preprint at <https://doi.org/10.48550/arXiv.1412.6980>.

**Supplemental information**

**Chemical reaction neural networks**

**to map lithium-ion battery**

**thermal runaway gas generation**

**Jiabo Zhang, Changsheng Ma, Shuaiqi Liu, Qianzhen Guo, Shaoyan Liu, Peng Han, Zhen Huang, and Dong Han**

## Supplemental Notes

### Note S1. The evaporation of the electrolyte solvent

The evaporation of the electrolyte solvent is considered as one of the contributors of BVG. Despite the presence of inert gas, the internal pressure of the airtight jar increases due to two primary reasons, namely the evaporation of the electrolyte,  $P_{ele}$ , and subsequent side chemical reactions during TR,  $P_g$ . The partial pressure of the airtight jar before  $T_2$  due to  $P_{ele}$  and  $P_g$  are plotted as a function of temperature in Figure S1. Specifically, without gas generation due to side reactions,  $P_{ele}$  is assumed to be equal to the saturation pressure of the electrolyte at the vapor-liquid equilibrium (VLE),  $P_{sat}$ , as represented by Eq. 1.

$$P_{ele} = P_{sat} = e^{a - \frac{b}{T - c}}, \quad (1)$$

where  $P_{sat}$  obeys Antoine's equation [1, 2] with  $a = -1.617$ ,  $b = 74.86$ , and  $c = 309.55$  for the present set of data.

### Note S2. Species evolution

Figure S3 depicted the species evolution of the LIB self-heating and violent TR processes for cells with initial SOs of 120%, 70%, and 50%, which show similar trends with that of SOC 100% condition.

### Note S3. The repeatability of the experiments

The repeatability of the experiments in this study is thoroughly evaluated through the repetition of each test at least three times. Figure S4 displays the temperature rise rate,  $dT/dt$ , as a function of temperature across four distinct tests for NCM cells with 100% SOC. It is evident that  $dT/dt$  for these experiments are nearly identical. Key parameters, including the onset temperature for TR ( $T_1$ ), separator collapsing temperature ( $T_2$ ), and the maximum temperature rise rate ( $(dT/dt)_{max}$ ), remain almost consistent across the four tests.

#### Note S4. The number of species and reactions

The dependence of minimum gas and mass loss values for the test datasets on the number of proposed species and reactions is depicted in Figures S5 A and B, respectively. It is evident that the prediction of gas and mass loss achieves the best-fit performance during the combination of 7 species and 8 reactions for the self-heating process, along with another 8 reactions for the violent TR process.

#### Supplemental Figures

**Figure S1. Partial Pressure due to the Evaporation of the Electrolyte Solvent**

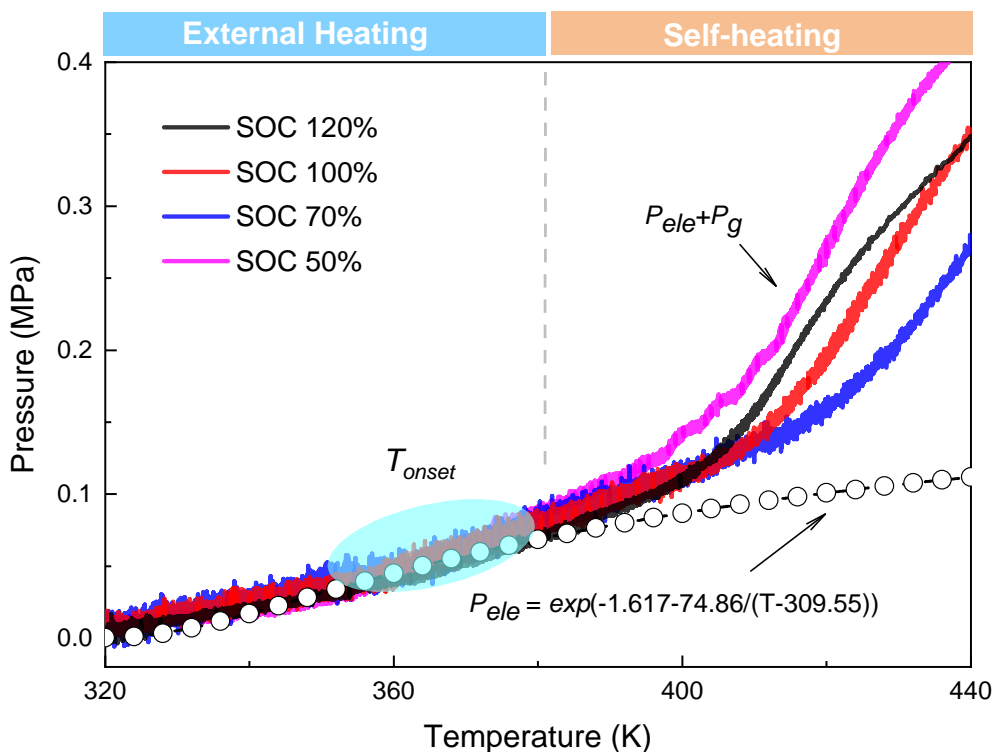


Figure S1: The partial pressure due to  $P_{ele}$  and  $P_g$  as a function of temperature for NCM cells with different SOCs, modified from [3].

## Figure S2. Learned CRNN weights and biases

(A) Chemical reaction kinetics parameters of the self-heating process.

(B) Chemical reaction kinetics parameters of the violent thermal runaway process.

**A**

LIB_in	Stoichiometric coefficients of reactants					Arrhenius parameters			Stoichiometric coefficients					
	S2_in	S3_in	S4_in	S5_in	Li+	Ea	b	InA	LIB	S2	S3	S4	S5	BVG
0.083	0.000	0.000	0.000	0.000	0.107	66.261	0.115	6.887	-0.083	0.045	0.002	0.004	0.009	0.023
0.119	0.000	0.000	0.000	0.000	0.136	63.782	0.149	7.012	-0.119	0.078	0.009	0.008	0.002	0.020
0.010	0.000	0.012	0.015	0.019	0.095	63.432	0.145	6.933	-0.010	0.033	-0.012	-0.015	-0.019	0.023
0.012	0.000	0.012	0.006	0.006	0.095	67.211	0.106	6.741	-0.012	0.018	-0.012	-0.006	-0.006	0.019
0.000	0.000	0.019	0.013	0.006	0.110	65.230	0.142	6.904	0.000	0.017	-0.019	-0.013	-0.006	0.020
0.024	0.000	0.019	0.013	0.000	0.103	63.508	0.100	6.952	-0.024	0.023	-0.019	-0.013	0.002	0.031
0.014	0.000	0.017	0.013	0.000	0.098	66.846	0.119	6.644	-0.014	0.011	-0.017	-0.013	0.010	0.023
0.030	0.000	0.021	0.014	0.005	0.126	60.876	0.142	6.911	-0.030	0.032	-0.021	-0.014	-0.005	0.038

**B**

LIB_in	S2_in	S3_in	S4_in	S5_in	Li+	Ea	b	InA	LIB	S2	S3	S4	S5	BVG
0.117	0.000	0.000	0.000	0.000	0.146	47.591	0.191	5.828	-0.117	0.000	0.000	0.005	0.000	0.112
0.093	0.000	0.000	0.000	0.000	0.122	48.255	0.150	5.532	-0.093	0.000	0.000	0.005	0.000	0.088
0.000	0.000	0.000	0.000	0.013	0.111	49.966	0.101	5.322	0.000	0.013	0.000	0.000	-0.013	0.000
0.000	0.011	0.000	0.000	0.000	0.119	50.362	0.089	5.381	0.000	-0.011	0.000	0.000	0.011	0.000
0.000	0.000	0.000	0.013	0.000	0.106	50.826	0.082	5.237	0.000	0.011	0.000	-0.013	0.001	0.000
0.047	0.019	0.000	0.000	0.000	0.140	48.742	0.148	5.621	-0.047	-0.019	0.000	0.000	0.012	0.053
0.000	0.016	0.000	0.000	0.000	0.120	50.204	0.070	5.356	0.000	-0.016	0.000	0.015	0.000	0.000
0.000	0.015	0.000	0.000	0.000	0.100	51.227	0.084	5.291	0.000	-0.015	0.000	0.000	0.015	0.000

Figure S2: Learned CRNN weights and biase.

**Figure S3. Species Profiles of TR process for LIBs with Different SOCs**

(A) and (B): 120%SOC

(C) and (D): 70%SOC

(E) and (F): 50%SOC

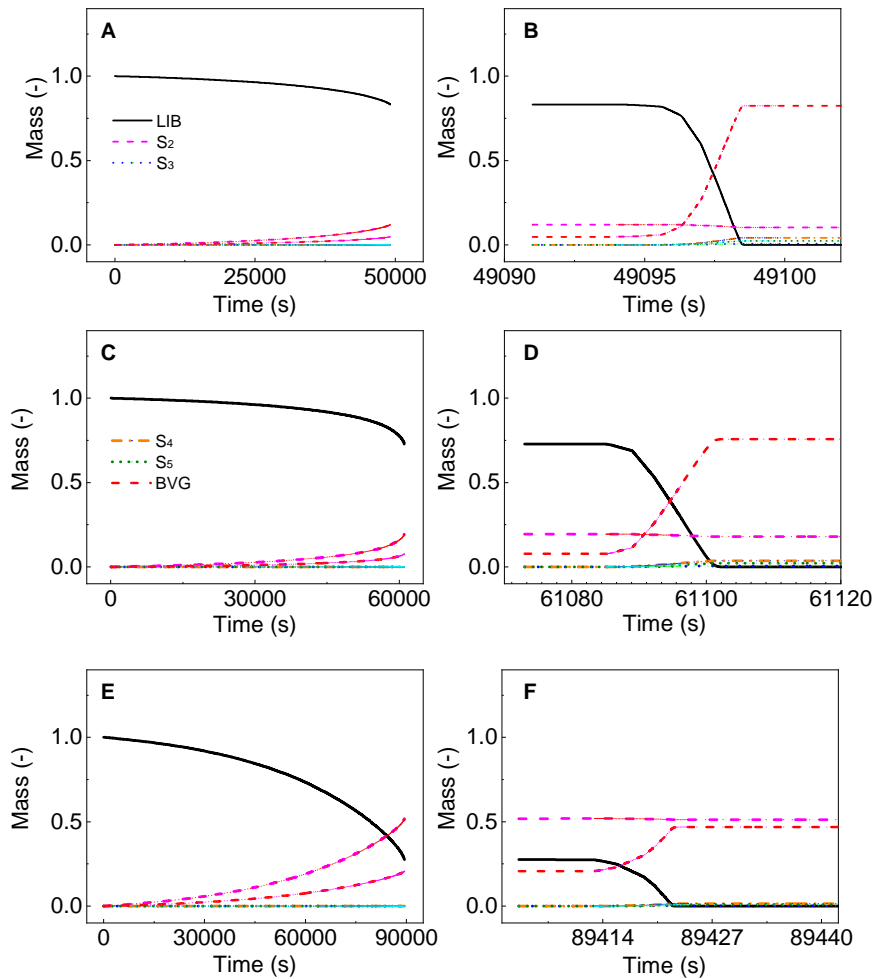


Figure S3: Species profiles of self-heating and violent TR process using the learned kinetic mechanism for LIBs.

**Figure S4. Repeatability of the Experimental Results**

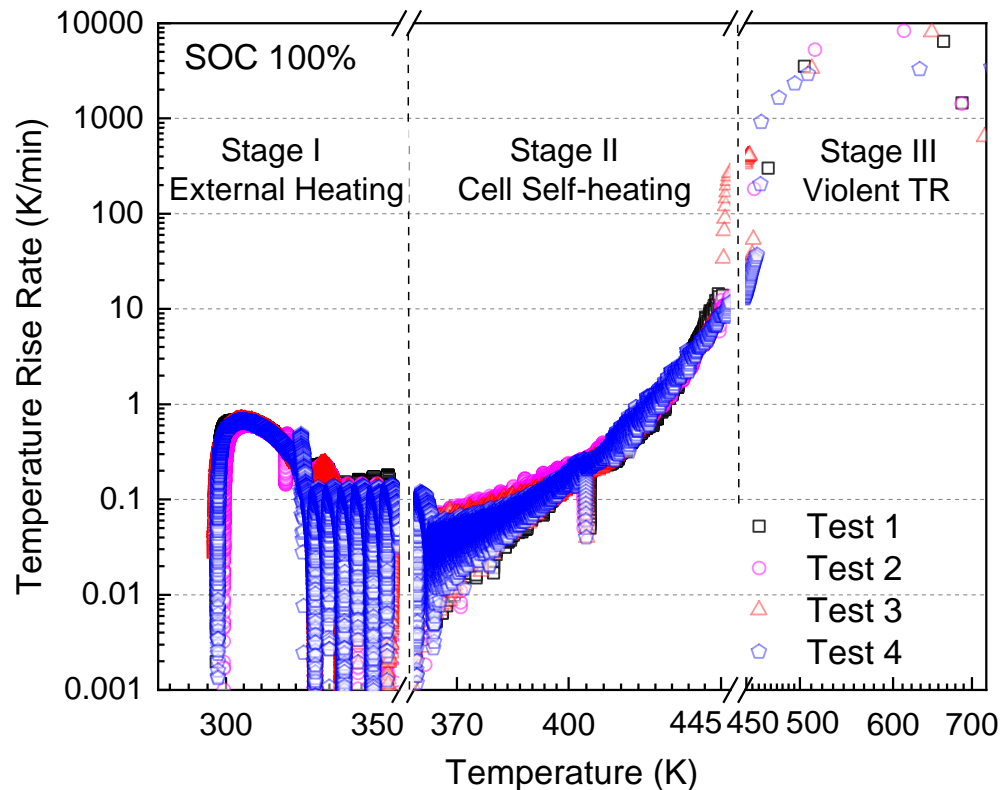


Figure S4: Comparison of the evolution of temperature rise rate,  $dT/dt$ , for NCM cells with 100% SOC during thermal runaway between different tests.

**Figure S5. Heat Map of the Minimum Gas and Mass Loss Values for the Test Datasets**

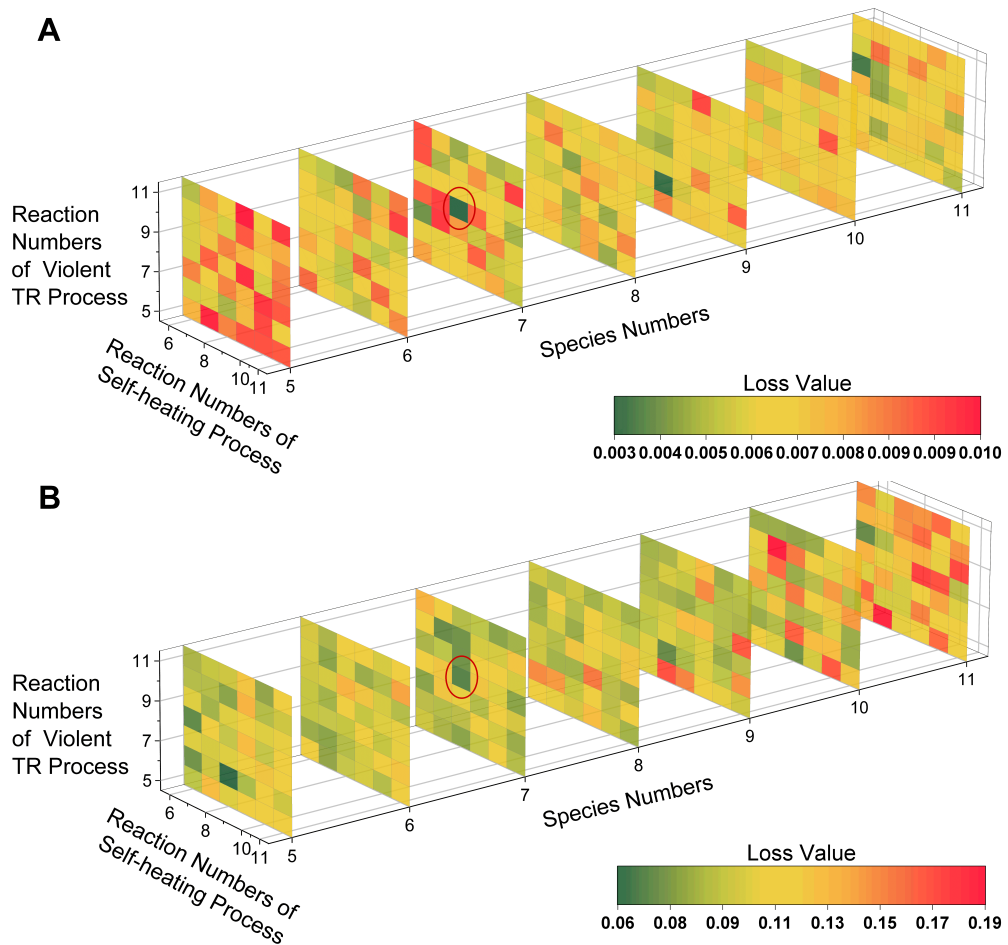


Figure S5: Heat map of the dependence of minimum loss functions for the test datasets on the number of proposed species and reactions.

## Nomenclature List

### Nomenclature

$b$	non-exponential temperature dependence factor
$\mathbf{Y}_0$	vector containing the initial concentrations
$\hat{\mathbf{m}}$	initial mass concentration vector
$\hat{\mathbf{m}}(t)$	vector of all species concentrations at each time step
$\hat{\mathbf{m}}_{gas}$	mass of venting gas
$\hat{\mathbf{m}}_{res}$	mass of solid residuals
$\mathbf{w}$	weights
$\mathbf{x}$	input to the neuron
$\mathbf{x}_i$	production rate of each species
$\sigma(\cdot)$	nonlinear activation function
$A$	pre-factor
$b$	bias
$E_a$	activation energy
$n_2$	gas generation amount at separator collapsing timing

$n_3$	maximum gas generation amount
$P_3$	maximum pressure
$T$	cell temperature
$T_0$	initial temperature
$T_1$	onset temperature
$T_2$	separator collapsing temperature
$t_2$	separator collapsing timing
$T_3$	maximum temperature
$v'_i$	stoichiometric coefficients of the reactants
$v''_i$	stoichiometric coefficients of the products
$y$	output of the neuron
$\bar{M}$	mean molar weight
$\hat{m}_2$	initial mass concentration vector for the violent TR process
$Li^+$	concentrations of active lithium within the cathode
$n$	the molar number of battery venting gas
<b>ARC</b>	accelerating rate calorimeter
<b>BVG</b>	battery venting gas
<b>CRNN</b>	chemical reaction neural network

<b>DEC</b>	diethyl carbonate
<b>EC</b>	ethylene carbonate
<b>EMC</b>	ethyl methyl carbonate
<b>GC</b>	gas chromatograph
<b>H-W-S</b>	heat-wait-seek
<b>ISC</b>	internal short circuit
<b>LFP</b>	$\text{LiFePO}_4$
<b>LIB</b>	lithium-ion battery
<b>LMO</b>	$\text{LiMn}_2\text{O}_4$
<b>MAE</b>	mean absolute error
<b>MVN</b>	molar value network
<b>NCM</b>	$\text{LiNi}_x\text{Co}_y\text{Mn}_z\text{O}_2$
<b>SEI</b>	solid electrolyte interface
<b>SOC</b>	state of charge
<b>TR</b>	thermal runaway

## References

- [1] P. T. Coman, S. Mátéfi-Tempfli, C. T. Veje, R. E. White, Modeling vaporization, gas generation and venting in li-ion battery cells with a dimethyl carbonate electrolyte, *J. Electrochem. Soc.* 164 (9) (2017) A1858.
- [2] P. Qin, J. Sun, Q. Wang, A new method to explore thermal and venting behavior of lithium-ion battery thermal runaway, *J. Power Sources* 486 (2021) 229357.
- [3] J. Zhang, Q. Guo, S. Liu, C. Zhou, Z. Huang, D. Han, Investigation on gas generation and corresponding explosion characteristics of lithium-ion batteries during thermal runaway at different charge states, *J. Energy Storage* 80 (2024) 110201. [doi:<https://doi.org/10.1016/j.est.2023.110201>](https://doi.org/10.1016/j.est.2023.110201).